

Charge-Transfer Plasmon Polaritons at Graphene/ α -RuCl₃ Interfaces

Daniel J. Rizzo, Bjarke S. Jessen, Zhiyuan Sun, Francesco L. Ruta, Jin Zhang, Jia-Qiang Yan, Lede Xian, Alexander S. McLeod, Michael E. Berkowitz, Kenji Watanabe, Takashi Taniguchi, Stephen E. Nagler, David G. Mandrus, Angel Rubio, Michael M. Fogler, Andrew J. Millis, James C. Hone, Cory R. Dean, and D. N. Basov*

Cite This: *Nano Lett.* 2020, 20, 8438–8445

Read Online

ACCESS |

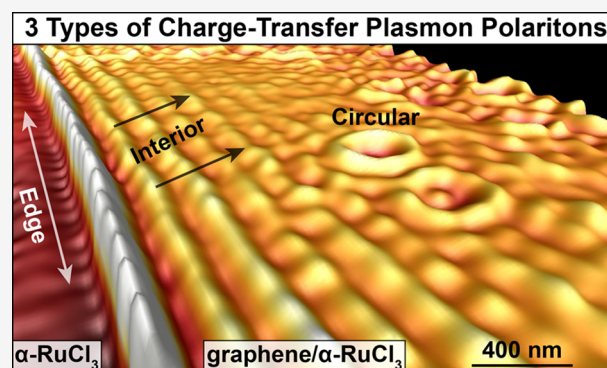
Metrics & More

Article Recommendations

Supporting Information

ABSTRACT: Nanoscale charge control is a key enabling technology in plasmonics, electronic band structure engineering, and the topology of two-dimensional materials. By exploiting the large electron affinity of α -RuCl₃, we are able to visualize and quantify massive charge transfer at graphene/ α -RuCl₃ interfaces through generation of charge-transfer plasmon polaritons (CPPs). We performed nanoimaging experiments on graphene/ α -RuCl₃ at both ambient and cryogenic temperatures and discovered robust plasmonic features in otherwise ungated and undoped structures. The CPP wavelength evaluated through several distinct imaging modalities offers a high-fidelity measure of the Fermi energy of the graphene layer: $E_F = 0.6$ eV ($n = 2.7 \times 10^{13}$ cm⁻²). Our first-principles calculations link the plasmonic response to the work function difference between graphene and α -RuCl₃ giving rise to CPPs. Our results provide a novel general strategy for generating nanometer-scale plasmonic interfaces without resorting to external contacts or chemical doping.

KEYWORDS: plasmon polaritons, α -RuCl₃, graphene, scanning near-field optical microscopy (SNOM), two-dimensional (2D) materials, Mott insulators



INTRODUCTION

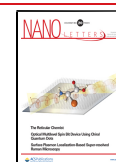
Research in two-dimensional (2D) materials has generated a library of tailor-made atomically thin layers whose optoelectronic properties are dictated by their lattice symmetry and elemental composition. The behavior of 2D materials can be further controlled via chemical or electrostatic doping.^{1,2} Moreover, van der Waals (vdW) heterostructures show emergent behavior based on interfacial effects, including orbital hybridization,^{3–5} magnetic interactions,⁶ and proximal superconductivity.⁷ Work function-mediated interlayer charge transfer offers another route to realizing novel interfacial phenomena.^{8–11} Specifically, the large work function of α -RuCl₃ ($\Phi_{\text{RuCl}_3} = 6.1$ eV)⁸ compared to graphene ($\Phi_g = 4.6$ eV)¹² is predicted to prompt interlayer charge transfer that creates in excess of $n = 10^{13}$ cm⁻² holes and electrons in graphene and α -RuCl₃, respectively. Such large charge carrier densities will likely impact the correlated insulating ground state of α -RuCl₃.^{13–18} Simultaneously, this interlayer charge transfer should metalize graphene, giving rise to plasmon polaritons without the need of electrical contacts or chemical alteration (as required previously), herein called charge-transfer plasmon polaritons (CPPs) (distinct from similarly named effects in coupled metallic nanoparticles).¹⁹ These hybrid light-matter modes formed by infrared photons and

Dirac electrons can travel over macroscopic distances in structures with high mobility.^{20–22}

Here, we harness CPPs to visualize and quantify charge transfer at the graphene/ α -RuCl₃ interface. The CPP wavelength is dictated by the electron density in the host medium, allowing us to read the strength of the charge transfer and the associated Fermi energy (E_F) in graphene/ α -RuCl₃ heterostructures directly from CPP images. The totality of CPP imaging data allows us to map the nanoscale spatial dependence of the interlayer charge transfer throughout the graphene/ α -RuCl₃ interface. Moreover, the electric field of the polaritonic wave extends over tens of nanometers outside of the graphene plane and provides access to the charge dynamics in effectively doped α -RuCl₃.

A polaritonic probe of graphene/ α -RuCl₃ heterostructures is enabled by scattering-type scanning near-field optical microscopy (s-SNOM), which permits us to map the near-field

Received: August 26, 2020
Revised: November 2, 2020
Published: November 9, 2020



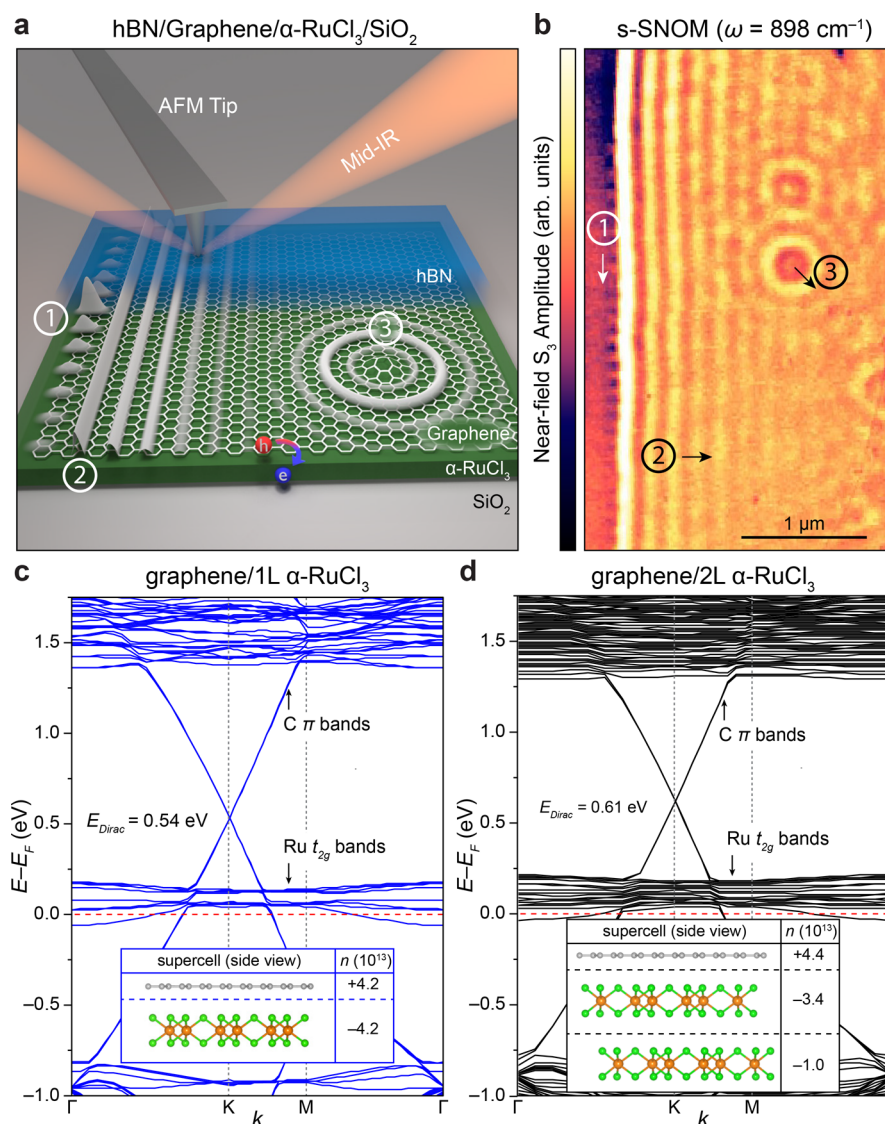


Figure 1. Characterization of interlayer charge transfer in graphene/ α -RuCl₃ heterostructures using s-SNOM and DFT calculations. (a) Diagram of s-SNOM performed on hBN/graphene/ α -RuCl₃/SiO₂. The large interlayer charge transfer creates the necessary conditions for generating three types of plasmon features: (1) edge CPPs, (2) CPPs, and (3) circular CPPs. (b) Map of the near-field amplitude near the edge of graphene in hBN/graphene/ α -RuCl₃/SiO₂ ($\omega = 898 \text{ cm}^{-1}$, $T = 60 \text{ K}$) showing oscillations that are characteristic of the three features shown in (a). (c) First-principles band structure with Hubbard U terms and including spin–orbital coupling for graphene/1L α -RuCl₃ (supercell shown in the inset). Bands derived from carbon π -orbitals and Ru t_{2g} orbital are indicated. Inset: The calculated Bader charge in each layer of the model supercell is indicated in terms of the resulting charge carrier concentration, n in units of cm^{-2} . (d) Same as (c) but for graphene/2L α -RuCl₃. Here, the interfacial layer of α -RuCl₃ possesses >70% of the electrons transferred from graphene.

optical response of this interface at subdiffractional length scales.²³ Thus, s-SNOM is well suited to image CPP waves over a wide range of IR frequencies (here, $\omega = 900\text{--}2300 \text{ cm}^{-1}$). Nanoimaging has allowed us to reconstruct the energy momentum dispersion $\omega(q_1)$ of CPPs prompted by an exceptionally high charge-carrier density in graphene ($n = 2.7 \times 10^{13} \text{ cm}^{-2}$, $E_F = 0.6 \text{ eV}$). Further analyses of both edge and circular CPPs (defined in Figure 1a,b) provide additional insight into the nanoscale spatial dependence of interlayer charge transfer and reveal sharp boundaries in the local optical conductivity. Finally, we evaluated the response function of doped α -RuCl₃ by modeling the complex CPP wavevector $\mathbf{q} = \mathbf{q}_1 + i\mathbf{q}_2$ and its variation with frequency and temperature. Here, \mathbf{q}_1 encodes information about the plasmon wavelength ($\lambda_p = 2\pi/q_1$), while \mathbf{q}_2 characterizes the plasmon damping. We observe CPP scattering that is consistent with an emergent

electronic response in the topmost layer of doped α -RuCl₃ at infrared frequencies deep below its band gap. DFT analysis confirms that it is primarily the interfacial layer of α -RuCl₃ that is impacted by charge transfer.

■ SEEING CHARGE-TRANSFER PLASMON POLARITONS

In order to explore the charge dynamics of the graphene/ α -RuCl₃ interface, we first constructed a graphene/ α -RuCl₃ heterostructure on a SiO₂/Si substrate encapsulated with hexagonal boron nitride (hBN) as shown in Figure 1a (see Supporting Information and Figure S1 for assembly details). Nano-IR images for graphene/ α -RuCl₃ heterostructures reveal three distinct but related forms of polaritonic waves (Figure 1b). Here, oscillations in the near-field amplitude are observed propagating inward from the graphene boundary that are

characteristic of CPPs. We also observe CPP fringes emanating radially from pointlike ($r < 50$ nm, $h \sim 1$ nm) topographic defects that appear to be acting as local plasmon reflectors, herein referred to as circular CPPs. Finally, we observed edge CPP fringes oscillating along the graphene edge. For pristine graphene, the plasmon wavelength, $\lambda_p \sim E_F^{-1/2}$, and can be used as a rough but straightforward measure of the interlayer charge transfer.²⁴ Here, all three imaging modalities produce a consistent estimate of $E_F = 0.5$ – 0.6 eV induced by charge transfer. Self-consistent DFT+U calculations on isolated α -RuCl₃ (Figure S2) and two heterostructures containing one (1L) and two (2L) layers of α -RuCl₃ (Figure 1c,d) yield similarly large values of E_F relative to that of pristine graphene (0.54 and 0.61 eV, respectively). Together, these observations reveal that the work function difference between graphene and α -RuCl₃ is sufficient to provide the conditions for generating prominent CPPs and potentially dope interfacial α -RuCl₃ into new physical regimes.

■ QUANTIFYING INTERFACIAL CHARGE DYNAMICS WITH CPPS

We proceed with our quantitative analysis of the CPP fringes visualized over a wide range of frequencies in the mid-IR using s-SNOM (Figure 2a,b). No such fringes were observed for graphene residing directly on SiO₂ (Figure S3), suggesting that this behavior originates from the graphene/ α -RuCl₃ interface. The CPP wavelength reveals a systematic variation with the incident laser frequency, ω , uncovering the dispersion $\omega(q_1)$ of these modes (Figure 2b). By fitting the average line profile of the CPP fringes (Figure S4),^{21,25} we are able to extract the

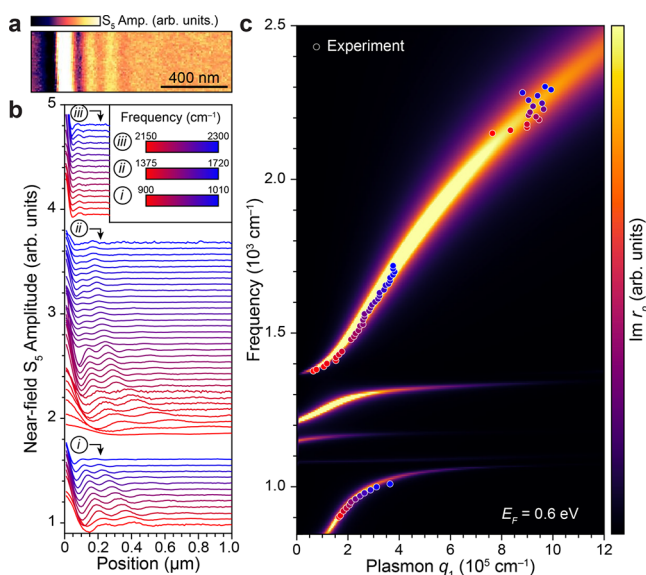


Figure 2. Characterization of the CPP dispersion in graphene/ α -RuCl₃ heterostructures using s-SNOM. (a) Map of the near-field amplitude ($\omega = 960$ cm⁻¹) near a graphene edge in graphene/ α -RuCl₃, showing CPP fringes. (b) Line profiles of the average near-field amplitude as a function of distance from the graphene edge for $\omega = 900$ – 2300 cm⁻¹, showing substantial shifts in the CPP wavelength. Here, sequential curves are offset vertically for clarity and grouped based on the three different ranges of frequencies labeled in the inset. (c) Dots: Plots of the experimental CPP dispersion derived from fits to the line profiles shown in (b) (Figure S4). The experimental data is superimposed on our best-fit theoretical model of $\text{Im } r_p$, with $E_F = 0.6$ eV.

dispersion for CPPs at the graphene/ α -RuCl₃ interface (Figure 2c). The experimental dispersion shows two branches: a lower branch in the frequency range 900 – 1010 cm⁻¹ and an upper branch spanning 1380 – 2300 cm⁻¹; the two branches are separated by a region of SiO₂ and hBN phonons, in accord with prior results.²⁶

An evident novelty of the data shown in Figure 2 is that the CPP dispersion is achieved without resorting to either gating or chemical doping. The appearance of CPP fringes in graphene/ α -RuCl₃ therefore attests to substantial charge transfer between graphene and α -RuCl₃. We are able to refine our extraction of E_F (i.e., the interlayer charge transfer) from the CPP behavior by modeling the precise dielectric environment of the graphene. Specifically, we calculate the theoretical plasmon dispersion from the p-polarized Fresnel reflection coefficient (r_p) and compared it to the experimental $\omega(q_1)$ plasmon dispersion. Our model properly accounts for the response functions and thicknesses of all constituent layers in the encapsulated graphene/ α -RuCl₃ heterostructure as described in the Supporting Information. Multilayer calculations of $\text{Im } r_p$ validate that the dominant contribution to the nano-optical response originates from plasmons in the graphene layer. A least-squares regression between the experimental dispersion and maxima in $\text{Im } r_p$ yields the graphene E_F as a fitting parameter (Figures 2c, S5). The model captures all of the trends in the data with the best-fit value of $E_F = 0.6$ eV corresponding to $n = 2.7 \times 10^{13}$ cm⁻² carriers in the graphene layer due to interlayer charge transfer (Figure 2c). This value is consistent with previous measurements of the Hall resistance ($n = 2.8 \times 10^{13}$ cm⁻²)⁸ and is in good agreement with theoretical expectation (Figure 1c,d).²⁷ We note that the agreement between the experimental and model dispersions was improved by assuming that the topmost layer of α -RuCl₃ possesses additional optical conductivity (Figure S5) compared to that of undoped α -RuCl₃.²⁸ Hence, our data establish the notion of large interfacial doping and enhanced optical conductivity in α -RuCl₃ as suggested by DFT calculations (Figure 1c,d).

While graphene/ α -RuCl₃ CPP fringes were primarily observed launching and reflecting from the graphene boundary, the interior of graphene reveals a different type of plasmonic oscillations exactly centered around topographic point defects (Figure S6a,b). We posit that these latter circular CPPs reflect off of these defects, forming radially symmetric $\lambda_p/2$ fringe patterns in the near-field amplitude. The lack of additional λ_p modulations to the circular CPP fringe pattern suggests that defects only act as reflectors of polaritonic waves but not as launchers. Detailed modeling corroborates this intuition (see Supporting Information for more details). Here, the defect is described as a small ($r \sim 40$ nm) region with a variable conductivity relative to the uniform areas in the interior of the sample (Figure S6c,d), while the near-field amplitude is approximated by a position-dependent reflectivity for illuminating fields from a raster-scanned point dipole. We observe that the sign and magnitude of the primary circular CPP fringe depend on the defect conductivity relative to that of the surrounding graphene. Conductivity-excess defects show a bright primary fringe, while conductivity-depletion defects show a dark primary fringe. A good fit to the experimental fringe cross-section can only be achieved with a maximally depleted (i.e., nonconducting) region at the defect site. Indeed, all defects in our data produce a dark primary fringe, consistent with the notion of depleted conductivity at the defect site. The

circular CPPs follow a dispersion that is similar to that of Figure 2c in the overlapping frequency region, implying that a similarly high level of hole density rapidly builds up away from the defect site (Figure S6e). Therefore, the near-field behavior of topographic defects reveals that they are sharp (nanometer-scale) undoped features surrounded by heavily doped graphene, consistent with a nanobubble in the graphene/ α -RuCl₃ interface.

The magnitude and spatial-dependence of the interlayer charge transfer between graphene and α -RuCl₃ revealed by s-SNOM experiments is further corroborated by Raman spectroscopy (Figure S7). Here, analysis of the graphene G and 2D peak shifts shows the coexistence of a highly doped ($n = 2.5 \times 10^{13} \text{ cm}^{-2}$), uniformly strained ($\epsilon = -0.2\%$) phase, and an undoped, randomly strained phase. The latter undoped phase only appears to be substantially represented in regions observed to have a high density of point defects (Figure S7).

Although bulk CPP dispersions act as sensitive probes of the interlayer charge transfer in the graphene interior, the edge CPP dispersion can provide information about the charge transfer profile near the boundary of graphene.²⁹ In order to exploit this, we extract the profiles of the near-field oscillations along the graphene edge as a function of ω (Figure 3a). The latter profiles correspond to $\lambda_p/2$ fringes generated by tip-launched edge CPPs reflecting off of notches in the graphene edge (Figures 3a, S4). As with the CPP fringes, the wavelength of the edge CPPs has a clear dependence on ω as shown in Figure 3b. As expected,^{30–32} edge CPPs possess a systematic

higher value of q_1 compared to CPPs in the interior (Figure 3b). Following the procedure in ref 29, we model the edge CPP dispersion based on the assumption of an abrupt boundary in the graphene conductivity coinciding with the graphene edge. This shows good agreement with experiment (Figure 3b). We remark that edge plasmons in graphene are a relatively rare sighting as they are likely to be smeared by electric field fringing in structures with relatively thick gate insulators and they have previously suffered dephasing when scattered by edge roughness.

EMERGENT ELECTRONIC RESPONSE OF INTERFACIAL α -RUCL₃

In order to accurately account for the depth of interlayer charge transfer in our modeling of the graphene/ α -RuCl₃ optical response, we revisit the first-principles calculations shown in Figure 1c,d. Analysis of the Bader charge³³ of both 1L and 2L structures shows that the graphene is heavily doped regardless of the number of α -RuCl₃ layers in our heterostructures. In principle, the graphene- α -RuCl₃ charge transfer can be tuned with the incorporation of hBN spacer layers (Figure S2). At the same time, the interfacial layer of α -RuCl₃ is nearly as heavily doped in the 2L structure as it is in the 1L structure (0.069 versus 0.056 $|e|/\text{Ru atom}$, respectively), while the second layer of α -RuCl₃ receives <30% of the electrons of the first (Figure 1c,d). Therefore, only the topmost interfacial layer of α -RuCl₃ is sufficiently doped to experience significant changes of the optoelectronic response, while subsequent layers more closely resemble the undoped bulk electronic structure. For every theoretical graphene/ α -RuCl₃ heterostructure characterized in our study, Ru t_{2g} bands that are unoccupied in intrinsic α -RuCl₃ (Figure S2) become populated, raising the possibility of emergent metallicity in α -RuCl₃ doped via interlayer charge transfer. With this in mind, all models of the optical response of our stack presented in this text consider the possibility of emergent optical conductivity in the topmost layer of α -RuCl₃ (Figure S8).

We evaluate the optical response of the graphene/ α -RuCl₃ interface by comparing the experimentally derived plasmon quality factor to all known loss channels. The inverse of the CPP quality factor, Q^{-1} , can be expressed in terms of the effective dielectric environment²⁰ and the optical conductivity of the graphene/ α -RuCl₃ interface

$$Q^{-1} = \frac{q_2}{q_1} \approx \frac{\sigma_1}{\sigma_2} + \frac{\kappa_2}{\kappa_1} = \frac{\gamma(\omega)}{\omega} + \frac{\kappa_2}{\kappa_1} \quad (1)$$

where $\sigma = \sigma_1 + i\sigma_2$ is the complex optical conductivity of the graphene/ α -RuCl₃ interface and $\kappa = \kappa_1 + i\kappa_2$ is the effective dielectric of the environment of our stack excluding the interfacial graphene/ α -RuCl₃ layers. The frequency-dependent scattering rate ($\gamma(\omega)$) has additive components, which can be broadly attributed to either the graphene ($\gamma_g(\omega)$) or α -RuCl₃ ($\gamma_{\alpha\text{RuCl}_3}(\omega)$) side of the interface

$$\gamma(\omega) = \gamma_{\alpha\text{RuCl}_3}(\omega) + \gamma_g(\omega) \quad (2)$$

The plasmonic dissipation in graphene, $\gamma_g(\omega)$, is well understood, and at room temperature is dominated by phonons.²⁰ Pristine α -RuCl₃ is a moderate gap insulator with a vanishingly small electronic response at infrared frequencies and does not significantly impact plasmonic losses. Conceivably, additional scattering may emerge as a result of a nontrivial electronic response at the interfacial layer of α -RuCl₃, which in

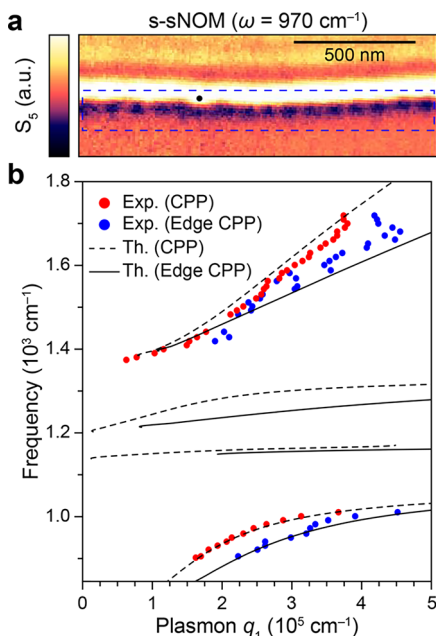


Figure 3. Analysis of the edge CPP dispersion in graphene/ α -RuCl₃ heterostructures. (a) Characteristic s-SNOM image ($\omega = 970 \text{ cm}^{-1}$) of edge CPP fringes along the graphene edge (highlighted by the dashed blue box). The fringe pattern shows $\lambda_p/2$ standing-waves formed by tip-launched edge plasmons reflecting off of notches in the graphene edge (such as that denoted by the solid black circle). (b) Red dots: The low-frequency CPP dispersion reproduced from Figure 2c. Blue dots: The edge CPP dispersion extracted from line profiles of the near-field amplitude along the graphene edge (see Figure S4). The dashed (solid) line shows the expected CPP (edge CPP) dispersion based on the assumption of a discontinuous jump in the graphene conductivity along that graphene edge (see Supporting Information).

turn should lead to a suppression of the experimental Q . With this in mind, we first extract the plasmon quality factor as a function of ω from the experimental fits to the CPP line profiles shown in Figure 2b, revealing a systematic decrease in Q with ω (Figure 4a). Using (1) along with known substrate optical parameters, the experimental Q can be used to obtain the combined scattering rate $\gamma(\omega)$ (Figure 4b). The contribution of graphene phonons to the scattering rate is shown in Figure 4b. Intrinsic scattering mechanisms in graphene fall short of the experimental values, revealing the

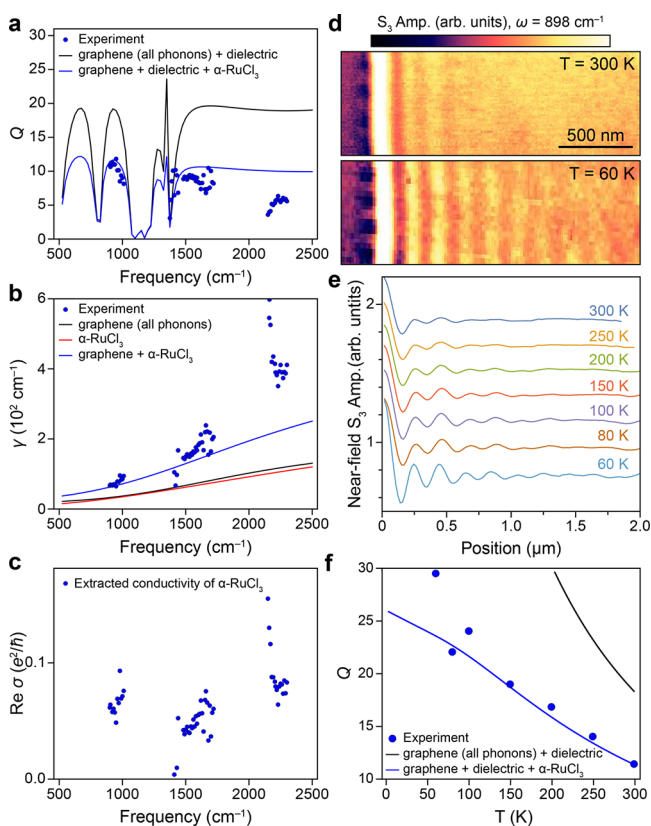


Figure 4. Temperature- and frequency-dependence of CPP losses in graphene/ α -RuCl₃ heterostructures. (a) Blue dots: Extracted quality factor, Q , for CPPs versus frequency. Black line: model Q versus ω for graphene phonon scattering and the dielectric environment only. Blue line: Same as the black line, plus model losses to the interfacial α -RuCl₃ layer. (b) Blue dots: The extracted γ versus ω derived from the experimental data in (a). Black line: The model γ versus ω based on graphene phonon scattering only. Red line: The model interfacial α -RuCl₃ scattering rate. Blue line: The total frequency-dependent scattering of the graphene and α -RuCl₃ layers. (c) The extracted optical conductivity of interfacial α -RuCl₃ based on the excess scattering observed in (b). (d) Map of the near-field amplitude ($\omega = 898 \text{ cm}^{-1}$) near a graphene edge in graphene/ α -RuCl₃ heterostructures taken at 300 K (top panel) and 60 K (bottom panel) under ultrahigh vacuum (UHV) conditions. (e) Line profiles of the average near-field amplitude as a function of distance from the graphene edge taken at the indicated sample temperatures ranging from 60–300 K. (f) Blue dots: The extracted CPP Q versus temperature taken from fits to the line profiles in (e) (see Figure S4). Black line: the model temperature-dependent Q based on graphene phonons and dielectric losses only. Blue line: Same as the black line, plus losses to the interfacial α -RuCl₃. For (a,f), the additional dielectric refers to losses attributable to all noninterfacial layers of the experimental stack shown in Figure S8 (i.e., the encapsulating hBN, bulk (undoped) α -RuCl₃ layers, and the underlying SiO₂).

presence of additional sources of scattering at the graphene/ α -RuCl₃ interface. While disorder is a potential source of scattering, such channels tend to produce frequency- and temperature-independent losses. The clear frequency dependence of the excess experimental scattering (i.e., beyond what is attributable to graphene) suggests that disorder alone does not offer an adequate description. Thus, we attribute the excess temperature- and frequency-dependent losses to emergent optical conductivity in the interfacial α -RuCl₃ altered by charge transfer. Our scattering analysis yields $\text{Re } \sigma_{\alpha\text{RuCl}_3}$ for the topmost layer of α -RuCl₃ in the range $0.02\text{--}0.1 e^2/h$ (Figure 4b,c). The small values of the extracted AC conductivity within the experimental frequency window suggest that interrogation of graphene/ α -RuCl₃ interfaces at lower frequencies is necessary to completely characterize the nature of the electronic response in doped α -RuCl₃ (i.e., fully localized versus itinerant charges). Nevertheless, the addition of an α -RuCl₃ loss channel greatly improves agreement between the theoretical and experimental scattering rates and quality factors (Figure 4a,b). The totality of these observations provides evidence that doped α -RuCl₃ possesses a nontrivial electronic response at infrared frequencies that acts as a damping mechanism for CPPs at the graphene side of the interface.

To further test the possibility of an emergent electronic response in doped α -RuCl₃, we obtained the temperature dependence ($T = 60\text{--}300 \text{ K}$) of the CPP damping rate for $\omega = 898 \text{ cm}^{-1}$ (Figures 4d,e). We observe that the Q -factor nearly triples as the sample temperature is brought from 300 K down to 60 K (Figure 4f). Once again, the calculated experimental scattering rate $\gamma(898 \text{ cm}^{-1}, T)$ is severely underestimated by phonon scattering and dielectric losses alone and is only reconciled with the model once the topmost layer of α -RuCl₃ is assumed to be endowed with an electronic response (Figures 4f, S9). The enhanced scattering rate at all observed temperatures therefore suggests the presence of electronic spectral weight at infrared frequencies in doped α -RuCl₃. While it was not possible to probe the DC transport of these carriers, a very small value of their AC conductivity suggests that these carriers may be either strongly correlated or localized.

OUTLOOK

The observations and analyses of CPPs presented in this work have broad implications in the study of α -RuCl₃, graphene plasmonics, and 2D materials generally. The recognition that massive charge transfer is taking place over macroscopic areas of graphene provides unambiguous validation of the notion that work function-mediated charge transfer can be used to “metallize” 2D materials into new physical regimes not attainable with common alternative methods. In the past, such high charge carrier densities in graphene could only be achieved with ion liquid gel devices, or an additional top-gate layer,³⁴ which add complexity to devices and forbid detailed surface studies with a scanning probe. Therefore, our experimental system provides a pathway for generating record high charge carrier densities at unobscured interfaces of 2D materials, which can, in principle, be further tuned with an additional backgate.^{8,10} Our findings indicate that it is now feasible to significantly dope 2D Mott insulators via work function mediated charge transfer. This is of particular interest for α -RuCl₃, which is predicted to host quantum spin liquids.

Furthermore, the observation that the graphene optical conductivity forms abrupt boundaries wherever the graphene/ α -RuCl₃ interface is interrupted suggests that α -RuCl₃ can be used to imprint nanoscale conductivity features in graphene and possibly other 2D materials without resorting to local back gates.³⁵ Similarly, patterned α -RuCl₃ arrays should offer a superior route to creating the sharp periodic potentials needed to realize graphene photonic crystals in gate-tunable graphene/semiconductor architectures.^{8,10,36} Concurrently, we have refined a procedure for probing the nanoscale optical response of 2D heterostructures across interfaces via the exploration of plasmon damping. This latter analysis hints at an enhanced electronic response in our doped interfacial α -RuCl₃ that needs to be verified with future direct measurements in the terahertz regime.

METHODS

Crystal Growth and Preparation. The hBN single crystals were grown using the temperature-gradient method using a Ba–BN solvent system. α -RuCl₃ crystals were grown by the sublimation of RuCl₃ powder sealed in a quartz tube under vacuum. About 1 g of powder was loaded in a quartz tube of 19 mm in outer diameter, 1.5 mm thick, and 10 cm long. The growth was performed in a box furnace. After dwelling at 1060 °C for 6 h, the furnace was cooled to 800 °C at a rate of 4 °C/h. Magnetic and specific heat measurements confirmed that the as-grown pristine crystal orders antiferromagnetically around 7 K. Graphene was derived from exfoliated highly oriented pyrolytic graphite.

Fabrication of Graphene/ α -RuCl₃ Heterostructures. The assembly of hBN/graphene/ α -RuCl₃ heterostructures was performed using standard dry-stacking methods.^{37,38} Because our near-field experiments require the encapsulating hBN crystal to be relatively thin (~3 nm), we opted for using a polycarbonate (PC) film on a polydimethylsiloxane (PDMS) support for the assembly. In our experience, the success rate with PC films is significantly higher than poly(propylene carbonate) (PPC) films when working with sub-5 nm 2D crystals.

To pick up the crystals, we manually bring the PC in contact with the SiO₂ substrate at ~90 °C using a micromanipulator. When the PC film is close (a few tens of micrometers) to the targeted crystal, we slowly increase the temperature to ~120 °C. As the temperature gradually increases, the thermal expansion allows the PC film to gradually and nondestructively cover the 2D crystals. By slowly lowering the temperature again, we can pick up the 2D crystals as the PC film retracts. This is performed sequentially on hBN and then graphene (Figure S1). The hBN/graphene stack is then positioned on top of the α -RuCl₃/SiO₂ to form the final heterostructure. The PC is then heated to 180 °C, which releases the film from the PDMS transfer slide and deposits it on the SiO₂. Finally, the PC film is removed in chloroform overnight.

Scanning Near-field Optical Microscopy. All s-SNOM measurements were performed on hBN-encapsulated graphene/ α -RuCl₃ on 285 nm SiO₂ on Si. We include a few layers of encapsulating hBN to protect the graphene surface from unwanted doping via atmospheric contaminants, complying with constraints of s-SNOM. The charge-transfer plasmon polariton (CPP) dispersion data was collected under ambient conditions on two commercial Neaspec systems using continuous wave quantum cascade lasers produced by Daylight Solutions. The temperature dependence of the plasmon

damping was measured in a home-built cryogenic s-SNOM using an 11 μ m CO₂ laser (Access Laser). s-SNOM experiments were conducted with an AFM operating in noncontact mode using metallic tips. Tapping frequencies of $f = 75$ and 285 kHz were used for ambient and UHV experiments, respectively. We demodulate the detected signal at the third (S₃) and fifth (S₅) harmonic of the tapping frequency in order to minimize background contributions to the backscattered near-field signal. A pseudoheterodyne interferometer is used to collect concurrent scattering amplitude and phase information from the near-field signal.

Modeling Charge-Transfer Plasmon Polaritons. A detailed description of the modeling employed for CPPs, edge CPPs, and circular CPPs is presented in the Supporting Information.

Ab Initio Calculations of Graphene/ α -RuCl₃ Heterostructures. The calculations were performed within the Vienna Ab initio Simulation Package (VASP)³⁹ using a projector-augmented wave (PAW) pseudopotential in conjunction with the Perdew–Burke–Ernzerhof (PBE)⁴⁰ functionals and plane-wave basis set with energy cutoff at 400 eV. A detailed description of all ab initio calculations is presented in the Supporting Information.

ASSOCIATED CONTENT

Supporting Information

The Supporting Information is available free of charge at <https://pubs.acs.org/doi/10.1021/acs.nanolett.0c03466>.

Detailed description of CPP modeling, heterostructure assembly, Raman spectroscopy, supplementary near-field measurements and DFT calculations (PDF)

AUTHOR INFORMATION

Corresponding Author

D. N. Basov – Department of Physics, Columbia University, New York, New York 10027, United States;
Email: db3056@columbia.edu

Authors

Daniel J. Rizzo – Department of Physics, Columbia University, New York, New York 10027, United States; orcid.org/0000-0003-4587-4863

Bjarke S. Jessen – Department of Physics and Department of Mechanical Engineering, Columbia University, New York, New York 10027, United States

Zhiyuan Sun – Department of Physics, Columbia University, New York, New York 10027, United States

Francesco L. Ruta – Department of Physics and Department of Applied Physics and Applied Mathematics, Columbia University, New York, New York 10027, United States;
orcid.org/0000-0002-8746-9420

Jin Zhang – Theory Department, Max Planck Institute for Structure and Dynamics of Matter and Center for Free-Electron Laser Science, 22761 Hamburg, Germany;
orcid.org/0000-0001-7830-3464

Jia-Qiang Yan – Materials Science and Technology Division, Oak Ridge National Laboratory, Oak Ridge, Tennessee 37831, United States; Department of Materials Science and Engineering, University of Tennessee, Knoxville, Tennessee 37996, United States

Lede Xian – Theory Department, Max Planck Institute for Structure and Dynamics of Matter and Center for Free-Electron Laser Science, 22761 Hamburg, Germany

Alexander S. McLeod – Department of Physics, Columbia University, New York, New York 10027, United States

Michael E. Berkowitz – Department of Physics, Columbia University, New York, New York 10027, United States; orcid.org/0000-0001-5962-2857

Kenji Watanabe – Research Center for Functional Materials, National Institute for Materials Science, Tsukuba 305-0044, Japan; orcid.org/0000-0003-3701-8119

Takashi Taniguchi – International Center for Materials Nanoarchitectonics, National Institute for Materials Science, Tsukuba 305-004, Japan; orcid.org/0000-0002-1467-3105

Stephen E. Nagler – Neutron Scattering Division, Oak Ridge National Laboratory, Oak Ridge, Tennessee 37831, United States

David G. Mandrus – Materials Science and Technology Division, Oak Ridge National Laboratory, Oak Ridge, Tennessee 37831, United States; Department of Materials Science and Engineering, University of Tennessee, Knoxville, Tennessee 37996, United States

Angel Rubio – Theory Department, Max Planck Institute for Structure and Dynamics of Matter and Center for Free-Electron Laser Science, 22761 Hamburg, Germany; Center for Computational Quantum Physics, Flatiron Institute, New York, New York 10010, United States; Nano-Bio Spectroscopy Group, Universidad del País Vasco UPV/EHU, San Sebastián 20018, Spain; orcid.org/0000-0003-2060-3151

Michael M. Fogler – Department of Physics, University of California San Diego, La Jolla, California 92093, United States

Andrew J. Millis – Department of Physics, Columbia University, New York, New York 10027, United States; Center for Computational Quantum Physics, Flatiron Institute, New York, New York 10010, United States

James C. Hone – Department of Mechanical Engineering, Columbia University, New York, New York 10027, United States

Cory R. Dean – Department of Physics, Columbia University, New York, New York 10027, United States

Complete contact information is available at:

<https://pubs.acs.org/10.1021/acs.nanolett.0c03466>

Author Contributions

D.J.R. and D.N.B. conceived and performed all near-field and Raman measurements. B.S.J., J.C.H., and C.R.D. assembled the heterostructures used for near-field experiments. D.J.R. and B.S.J. collated and analyzed near-field and Raman data. F.L.R. performed theoretical analysis of the surface CPP dispersion. Z.S. and A.J.M. performed theoretical analysis of the surface CPP damping rates. J.Z. performed all DFT calculations and analyzed the results with L.X. and A.R. J.-Q.Y., S.E.N., and D.G.M. synthesized and characterized α -RuCl₃ crystals. A.S.M. and M.E.B. performed theoretical modeling of circular plasmons. K.W. and T.T. synthesized and characterized hBN crystals used for encapsulation. M.M.F. performed theoretical analysis of the edge CPP dispersion.

Notes

The authors declare no competing financial interest.

ACKNOWLEDGMENTS

Research at Columbia was supported as part of the Energy Frontier Research Center on Programmable Quantum Materials funded by the U.S. Department of Energy (DOE), Office of Science, Basic Energy Sciences (BES), under Award No. DE-SC0019443. J.Z., L.X., and A.R. were supported by the European Research Council (ERC-2015-AdG694097), the Cluster of Excellence “Advanced Imaging of Matter” (AIM) EXC 2056 - 390715994, funding by the Deutsche Forschungsgemeinschaft (DFG, German Research Foundation) under RTG 2247, Grupos Consolidados (IT1249-19) and SFB925 “Light induced dynamics and control of correlated quantum systems”. J.Z. acknowledges funding received from the European Union Horizon 2020 research and innovation program under Marie Skłodowska-Curie Grant Agreement 886291 (PeSD-NeSL). J.Z., L.X., and A.R. would like to acknowledge Nicolas Tancogne-Dejean for fruitful discussions and also acknowledge support by the Max Planck Institute-New York City Center for Non-Equilibrium Quantum Phenomena. The Flatiron Institute is a division of the Simons Foundation. D.G.M. acknowledges support from the Gordon and Betty Moore Foundation’s EPIQS Initiative, Grant GBMF9069. Work at ORNL was supported by the U.S. Department of Energy, Office of Science, Basic Energy Sciences, Materials Sciences and Engineering Division. K.W. and T.T. acknowledge support from the Elemental Strategy Initiative conducted by the MEXT, Japan, Grant JPMXP0112101001, JSPS KAKENHI Grant JP20H00354, and the CREST (JPMJCR15F3), JST. S.E.N. was supported by the Division of Scientific User Facilities of the U.S. DOE Basic Energy Sciences. M.M.F. acknowledges support from the Office of Naval Research Grant N00014-18-1-2722. D.N.B. is the Vannevar Bush Faculty ONR-VB: N00014-19-1-2630 and Moore investigator in Quantum Materials EPIQS program #9455. A.S.M. acknowledges support from award 80NSSC19K1210 under the NASA Laboratory Analysis of Returned Samples program.

REFERENCES

- (1) Chen, X.; Zhou, Z.; Deng, B.; Wu, Z.; Xia, F.; Cao, Y.; Zhang, L.; Huang, W.; Wang, N.; Wang, L. Electrically tunable physical properties of two-dimensional materials. *Nano Today* **2019**, *27*, 99–119.
- (2) Keimer, B.; Moore, J. E. The physics of quantum materials. *Nat. Phys.* **2017**, *13*, 1045–1055.
- (3) Mele, E. J. Commensuration and interlayer coherence in twisted bilayer graphene. *Phys. Rev. B: Condens. Matter Mater. Phys.* **2010**, *81*, 161405.
- (4) Suarez Morell, E.; Correa, J. D.; Vargas, P.; Pacheco, M.; Barticevic, Z. Flat bands in slightly twisted bilayer graphene: Tight-binding calculations. *Phys. Rev. B: Condens. Matter Mater. Phys.* **2010**, *82*, 121407.
- (5) Xian, L.; Kennes, D. M.; Tancogne-Dejean, N.; Altarelli, M.; Rubio, A. Multiflat bands and strong correlations in twisted bilayer boron nitride: Doping-induced correlated insulator and superconductor. *Nano Lett.* **2019**, *19*, 4934–4940.
- (6) Zhong, D.; Seyler, K. L.; Linpeng, X.; Cheng, R.; Sivasdas, N.; Huang, B.; Schmidgall, E.; Taniguchi, T.; Watanabe, K.; McGuire, M. A.; Yao, W.; Xiao, D.; Fu, K.-M. C.; Xu, X. Van der Waals engineering of ferromagnetic semiconductor heterostructures for spin and valleytronics. *Science Advances* **2017**, *3*, No. e1603113.
- (7) Lundberg, M. B.; Gao, Y.; Asgari, R.; Tan, C.; Van Duppen, B.; Autore, M.; Alonso-González, P.; Woessner, A.; Watanabe, K.; Taniguchi, T.; Hillenbrand, R.; Hone, J.; Polini, M.; Koppens, F. H.

- L. Tuning quantum nonlocal effects in graphene plasmonics. *Science* **2017**, *357*, 187.
- (8) Zhou, B.; Balgley, J.; Lampen-Kelley, P.; Yan, J. Q.; Mandrus, D. G.; Henriksen, E. A. Evidence for charge transfer and proximate magnetism in graphene/ α -RuCl₃ heterostructures. *Phys. Rev. B: Condens. Matter Mater. Phys.* **2019**, *100*, 165426.
- (9) Hu, F.; Kim, M.; Zhang, Y.; Luan, Y.; Ho, K. M.; Shi, Y.; Wang, C. Z.; Wang, X.; Fei, Z. Tailored Plasmons in Pentacene/Graphene Heterostructures with Interlayer Electron Transfer. *Nano Lett.* **2019**, *19*, 6058–6064.
- (10) Mashhadi, S.; Kim, Y.; Kim, J.; Weber, D.; Taniguchi, T.; Watanabe, K.; Park, N.; Lotsch, B.; Smet, J. H.; Burghard, M.; Kern, K. Spin-Split Band Hybridization in Graphene Proximitized with α -RuCl₃ Nanosheets. *Nano Lett.* **2019**, *19*, 4659–4665.
- (11) Wang, Y.; Balgley, J.; Gerber, E.; Gray, M.; Kumar, N.; Lu, X.; Yan, J.-Q.; Fereidouni, A.; Basnet, R.; Yun, S. J. Modulation Doping via a 2D Atomic Crystalline Acceptor. *Nano Lett.* **2020**. <https://arxiv.org/abs/2007.06603> (accessed on July 13, 2020).
- (12) Yu, Y.-J.; Zhao, Y.; Ryu, S.; Brus, L. E.; Kim, K. S.; Kim, P. Tuning the Graphene Work Function by Electric Field Effect. *Nano Lett.* **2009**, *9*, 3430–3434.
- (13) Sears, J. A.; Songvilay, M.; Plumb, K. W.; Clancy, J. P.; Qiu, Y.; Zhao, Y.; Parshall, D.; Kim, Y.-J. Magnetic order in α -RuCl₃: A honeycomb-lattice quantum magnet with strong spin-orbit coupling. *Phys. Rev. B: Condens. Matter Mater. Phys.* **2015**, *91*, 144420.
- (14) Plumb, K. W.; Clancy, J. P.; Sandilands, L. J.; Shankar, V. V.; Hu, Y. F.; Burch, K. S.; Kee, H.-Y.; Kim, Y.-J. α -RuCl₃: A spin-orbit assisted Mott insulator on a honeycomb lattice. *Phys. Rev. B: Condens. Matter Mater. Phys.* **2014**, *90*, 041112.
- (15) Okamoto, S. Global phase diagram of a doped Kitaev-Heisenberg model. *Phys. Rev. B: Condens. Matter Mater. Phys.* **2013**, *87*, 064508.
- (16) Wu, L.; Little, A.; Aldape, E. E.; Rees, D.; Thewalt, E.; Lampen-Kelley, P.; Banerjee, A.; Bridges, C. A.; Yan, J. Q.; Boone, D.; Patankar, S.; Goldhaber-Gordon, D.; Mandrus, D.; Nagler, S. E.; Altman, E.; Orenstein, J. Field evolution of magnons in α -RuCl₃ by high-resolution polarized terahertz spectroscopy. *Phys. Rev. B: Condens. Matter Mater. Phys.* **2018**, *98*, 094425.
- (17) Banerjee, A.; Bridges, C. A.; Yan, J. Q.; Aczel, A. A.; Li, L.; Stone, M. B.; Granroth, G. E.; Lumsden, M. D.; Yiu, Y.; Knolle, J.; Bhattacharjee, S.; Kovrizhin, D. L.; Moessner, R.; Tennant, D. A.; Mandrus, D. G.; Nagler, S. E. Proximate Kitaev quantum spin liquid behaviour in a honeycomb magnet. *Nat. Mater.* **2016**, *15*, 733–740.
- (18) Gerber, E.; Yao, Y.; Arias, T. A.; Kim, E.-A. Ab Initio Mismatched Interface Theory of Graphene on α -RuCl₃: Doping and Magnetism. *Phys. Rev. Lett.* **2020**, *124*, 106804.
- (19) Wen, F.; Zhang, Y.; Gottheim, S.; King, N. S.; Zhang, Y.; Nordlander, P.; Halas, N. J. Charge Transfer Plasmons: Optical Frequency Conductances and Tunable Infrared Resonances. *ACS Nano* **2015**, *9*, 6428–6435.
- (20) Ni, G. X.; McLeod, A. S.; Sun, Z.; Wang, L.; Xiong, L.; Post, K. W.; Sunku, S. S.; Jiang, B. Y.; Hone, J.; Dean, C. R.; Fogler, M. M.; Basov, D. N. Fundamental limits to graphene plasmonics. *Nature* **2018**, *557*, 530–533.
- (21) Woessner, A.; Lundeberg, M. B.; Gao, Y.; Principi, A.; Alonso-González, P.; Carrega, M.; Watanabe, K.; Taniguchi, T.; Vignale, G.; Polini, M.; Hone, J.; Hillenbrand, R.; Koppens, F. H. L. Highly confined low-loss plasmons in graphene–boron nitride heterostructures. *Nat. Mater.* **2015**, *14*, 421–425.
- (22) Naik, G. V.; Shalae, V. M.; Boltasseva, A. Alternative Plasmonic Materials: Beyond Gold and Silver. *Adv. Mater.* **2013**, *25*, 3264–3294.
- (23) Atkin, J. M.; Berweger, S.; Jones, A. C.; Raschke, M. B. Nano-optical imaging and spectroscopy of order, phases, and domains in complex solids. *Adv. Phys.* **2012**, *61*, 745–842.
- (24) Luo, X.; Qiu, T.; Lu, W.; Ni, Z. Plasmons in graphene: recent progress and applications. *Mater. Sci. Eng., R* **2013**, *74*, 351–376.
- (25) Bosman, M.; Ye, E.; Tan, S. F.; Nijhuis, C. A.; Yang, J. K. W.; Marty, R.; Mlayah, A.; Arbouet, A.; Girard, C.; Han, M.-Y. Surface plasmon damping quantified with an electron nanoprobe. *Sci. Rep.* **2013**, *3*, 1312–1312.
- (26) Dai, S.; Ma, Q.; Liu, M.; Andersen, T.; Fei, Z.; Goldflam, M.; Wagner, M.; Watanabe, K.; Taniguchi, T.; Thiemens, M.; Keilmann, F.; Janssen, G.; Zhu, S.-E.; Jarillo-Herrero, P.; Fogler, M.; Basov, D. Graphene on hexagonal boron nitride as a tunable hyperbolic metamaterial. *Nat. Nanotechnol.* **2015**, *10*, 682–686.
- (27) Biswas, S.; Li, Y.; Winter, S. M.; Knolle, J.; Valentí, R. Electronic Properties of α -RuCl₃ in Proximity to Graphene. *Phys. Rev. Lett.* **2019**, *123*, 237201.
- (28) Götze, W.; Wölfle, P. Homogeneous Dynamical Conductivity of Simple Metals. *Phys. Rev. B* **1972**, *6*, 1226–1238.
- (29) Volkov, V.; Mikhailov, S. A. Edge magnetoplasmons: low frequency weakly damped excitations in inhomogeneous two-dimensional electron systems. *Sov. Phys. JETP* **1988**, *67*, 1639–1653.
- (30) Fei, Z.; Goldflam, M. D.; Wu, J. S.; Dai, S.; Wagner, M.; McLeod, A. S.; Liu, M. K.; Post, K. W.; Zhu, S.; Janssen, G. C. A. M.; Fogler, M. M.; Basov, D. N. Edge and Surface Plasmons in Graphene Nanoribbons. *Nano Lett.* **2015**, *15*, 8271–8276.
- (31) Nikitin, A. Y.; Alonso-González, P.; Vélez, S.; Mastel, S.; Centeno, A.; Pesquera, A.; Zurutuza, A.; Casanova, F.; Hueso, L. E.; Koppens, F. H. L.; Hillenbrand, R. Real-space mapping of tailored sheet and edge plasmons in graphene nanoresonators. *Nat. Photonics* **2016**, *10*, 239–243.
- (32) Gonçalves, P. A. D.; Xiao, S.; Peres, N. M. R.; Mortensen, N. A. Hybridized Plasmons in 2D Nanoslits: From Graphene to Anisotropic 2D Materials. *ACS Photonics* **2017**, *4*, 3045–3054.
- (33) Bader, R. F. W. Principle of stationary action and the definition of a proper open system. *Phys. Rev. B: Condens. Matter Mater. Phys.* **1994**, *49*, 13348–13356.
- (34) Das, A.; Pisana, S.; Chakraborty, B.; Piscanec, S.; Saha, S. K.; Waghmare, U. V.; Novoselov, K. S.; Krishnamurthy, H. R.; Geim, A. K.; Ferrari, A. C.; Sood, A. K. Monitoring dopants by Raman scattering in an electrochemically top-gated graphene transistor. *Nat. Nanotechnol.* **2008**, *3*, 210–215.
- (35) Alonso-González, P.; Nikitin, A. Y.; Gao, Y.; Woessner, A.; Lundeberg, M. B.; Principi, A.; Forcellini, N.; Yan, W.; Vélez, S.; Huber, A. J.; Watanabe, K.; Taniguchi, T.; Casanova, F.; Hueso, L. E.; Polini, M.; Hone, J.; Koppens, F. H. L.; Hillenbrand, R. Acoustic terahertz graphene plasmons revealed by photocurrent nanoscopy. *Nat. Nanotechnol.* **2017**, *12*, 31–35.
- (36) Xiong, L.; Forsythe, C.; Jung, M.; McLeod, A. S.; Sunku, S. S.; Shao, Y. M.; Ni, G. X.; Sternbach, A. J.; Liu, S.; Edgar, J. H.; Mele, E. J.; Fogler, M. M.; Shvets, G.; Dean, C. R.; Basov, D. N. Photonic crystal for graphene plasmons. *Nat. Commun.* **2019**, *10*, 4780.
- (37) Pizzocchero, F.; Gammelgaard, L.; Jessen, B. S.; Caridad, J. M.; Wang, L.; Hone, J.; Bøggild, P.; Booth, T. J. The hot pick-up technique for batch assembly of van der Waals heterostructures. *Nat. Commun.* **2016**, *7*, 11894.
- (38) Purdie, D. G.; Pugno, N. M.; Taniguchi, T.; Watanabe, K.; Ferrari, A. C.; Lombardo, A. Cleaning interfaces in layered materials heterostructures. *Nat. Commun.* **2018**, *9*, 5387.
- (39) Kresse, G.; Furthmüller, J. Efficient iterative schemes for ab initio total-energy calculations using a plane-wave basis set. *Phys. Rev. B: Condens. Matter Mater. Phys.* **1996**, *54*, 11169–11186.
- (40) Perdew, J. P.; Burke, K.; Ernzerhof, M. Generalized gradient approximation made simple. *Phys. Rev. Lett.* **1996**, *77*, 3865.